J|A|C|S ARTICLES

Published on Web 07/12/2010

Peroxo−Iron Mediated Deformylation in Sterol 14α-Demethylase Catalysis

Kakali Sen and John C Hackett*

Institute for Structural Biology and Drug Discovery, Virginia Commonwealth University, 800 East Leigh Street, Richmond, Virginia 23219

Received July 23, 2009; E-mail: jchackett@vcu.edu

Abstract: The mechanisms of cytochrome P450 (CYP) catalyzed C−C bond cleavage have been strongly debated and difficult to unravel. Herein, deformylation mechanisms of the sterol 14α-demethylase (CYP51) from *Mycobacterium tuberculosis* are elucidated using molecular dynamics simulation, density functional theory, and hybrid quantum mechanics/molecular mechanics methods. These results provide strong theoretical support for the operation of the peroxo intermediate in CYP-catalyzed deformylation. Molecular dynamics simulations support the lanosterol carboxaldehyde intermediate diverts the hydrogen-bonded network of water putatively involved in proton delivery to peroxo and compound **0** (Cmpd 0) away from the O_2 ligand. In the presence of the aldehyde substrate, the peroxo intermediate is trapped as the peroxohemiacetal without an apparent barrier, which may then be protonated in the active site. The unprotonated peroxohemiacetal provides a branch point for a concerted deformylation mechanism; however, a stepwise mechanism initiated by cleavage of the C−C bond was found to be more energetically feasible. Population analyses of the peroxoformate/deformylated substrate complex indicate that heterolytic cleavage of the C−C bond in the enzyme environment generates a carbanion at C14. Conversely, in the absence of the protein electrostatic background, the C−C cleavage reaction proceeds homolytically, indicating that the active site environment exerts a strong modulatory effect on the electronic structure of this intermediate. If the peroxohemiacetal is protonated, this species preferentially expels formic acid through an O−O cleavage transition state. After expulsion of the formyl unit, both proton-independent and -dependent pathways converge to a complex containing compound **II**, which readily abstracts the 15α-hydrogen, thereby inserting the 14,15 double bond into the steroid skeleton. Parallel studies considering nucleophilic addition of Cmpd 0 to the aldehyde intermediate indicated that this reaction proceeds with high energetic barriers. Finally, the hydrogen atom abstraction and proton coupled electron transfer mechanism (*J. Am. Chem. Soc.* **2005**, *127*, 5224−5237) for compound **I** (Cmpd I) mediated deformylation of the geminal diol was considered in the context of the protein environment. In contrast to gas phase calculations, triradicaloid and pentaradicaloid Cmpd I states failed to initiate a concerted deformylation of the geminal diol. This study provides a unified mechanistic view consistent with decades of experiments aimed at understanding the deformylation reaction. Additionally, these results provide general mechanistic insight into the catalytic mechanisms of several biosynthetic and xenobiotic-oxidizing CYP enzymes of biomedical importance.

1. Introduction

The cytochromes P450 (CYPs) generally use two reducing equivalents and O_2 to oxidize a myriad of organic compounds. These enzymes are involved in the disposition of xenobiotics and in the biosynthesis of endogenous compounds.[1,2] The generally accepted CYP catalytic cycle involves several reactive oxygen intermediates, illustrated in Scheme 1, having short lifetimes that pose difficulties for experimental characterization. Most CYPs catalyze regioselective insertion of oxygen atoms into inert C−H bonds, resulting in hydroxylated products. The consensus is that this reaction is mediated by the oxoferryl π-cation radical, also known as compound **I** (Cmpd I) and proceeds through a hydrogen-atom abstraction/hydroxyl radical rebound mechanism.[3,4] Nonetheless, this mechanism fails to account for the oxidative C−C bond cleavage observed in several CYP-catalyzed reactions.

Scheme 1

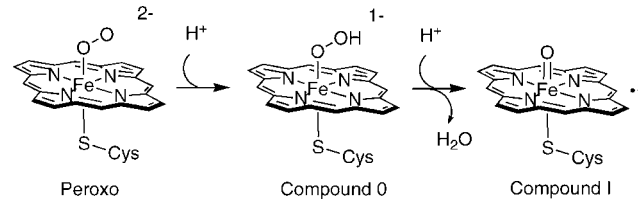

(1) Rendic, S. *Drug Metab. Rev.* **2002**, *34*, 83.
(2) Ortiz de Montellano, P. R. *Cytochrome P450: Structure, Mechanism, and Biochemistry*, 3rd ed.; Kluwer Academic/Plenum Publishers: New York, 2005.
(3) Groves, J. T.; McClusky, G. A. *J. Am. Chem. Soc.* **1976**, *98*, 859.
(4) Groves, J. T.; McClusky, G. A. *Biochem. Biophys. Res. Commun.* **1978**, *81*, 154.

Scheme 2

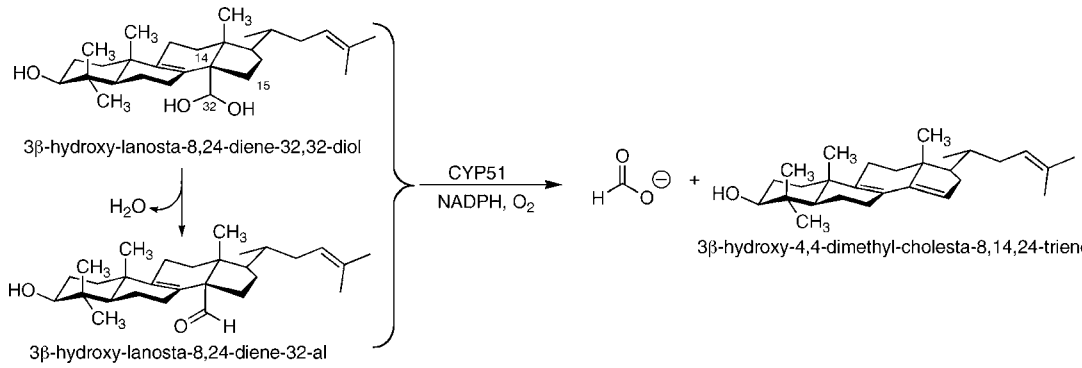

There are a number of CYP-catalyzed reactions known to cleave C−C bonds,[5−7] the most common being the deformylation of aldehydes.[8−10] Identities of the reactive oxygen intermediate(s) and the corresponding catalytic mechanism(s) have been controversial and difficult to unravel. The C−C cleaving CYPs use three equivalents each of NADPH and O_2 to cleave these bonds. In the case of deformylation, the first two steps entail methyl group hydroxylation, successively forming the alcohol and geminal diol, respectively.[8,9,11−14] The latter intermediate dehydrates to the aldehyde, which is oxidatively removed as formate. The sterol 14α-demethylases (CYP51) and aromatase (CYP19) enzymes catalyze this deformylation reaction in steroidogenesis. CYP51 is a validated target for treatment of fungal infections[15,16] Furthermore, the identification of CYP51 homologues in *Mycobacterium tuberculosis*, *Trypanosoma*, and *Leishmania* species has renewed interest in this enzyme for the development of novel therapeutics to treat these infections.[17−20] CYP19 catalyzes the oxidative deformylation and aromatization of androgens to estrogens, and hence, there has been longstanding interest in the mechanism of this enzyme for its role in estrogen-dependent breast carcinoma.[21,22] In the case of CYP51, deformylation results in expulsion of the 14α-methyl group as formate with concomitant introduction of a 14,15 double bond (Scheme 2). In each enzyme, deformylation occurs with steroselective removal of a hydrogen atom on the *syn* face of deformylation site. The stereochemistry of the deformylation step is consistent with the peroxo species as the active oxidant.[9,11] However, theoretical studies of the final catalytic step of aromatase revealed that Cmpd I effectively deformylates the geminal diol with low energetic barriers.[23] Despite overwhelming support for Cmpd I as the active oxidant in much of CYP catalysis, the peroxo species has been invoked to mediate the deformylation reaction in these enzymes; however, the catalytic mechanism has remained unclear.

A number of xenobiotic aldehydes are also deformylated by CYPs. Coon and co-workers demonstrated that a number of small molecular weight aldehydes were subject to deformylation to form olefin metabolites.[8] Furthermore, these investigators demonstrated that cyclohexane carboxaldehyde is converted to cyclohexene and formic acid. This reaction was supported by H_2O_2 rather than iodosobenzene, suggesting that the deformylation reaction is not attributable to Cmpd I.[10] Subsequently, it was shown that mutation of the conserved active site Thr302 in CYP2B4 decreased catalytic turnover of substrates undergoing putative Cmpd I dependent hydroxylation reactions while increasing the rate of cyclohexane decarboxylation 10-fold.[24] The mutation putatively disrupts the active site proton relay, thereby decreasing the availability of protons required for O−O cleavage. Consequently, the peroxo would be favored over Cmpd I, increasing the substrate deformylation rate.

The role of the peroxo species as an active oxidant is supported by studies incorporating heme- and non-heme-peroxo organoiron complexes.[25−28] Wertz and co-workers demonstrated that a ferric tetramesitylporphyrin peroxo complex reacts with 4-androsten-3,17-dione-19-al, an aromatase substrate, to produce the 4,5-epoxide. However, when the A ring of this substrate was trapped as an enol triflate, the reaction generates the same deformylated products observed in the enzyme-catalyzed transformation.[26] The ferric peroxo complex has also been generated with several non-heme tetradentate ligands (L) [(L = TMC, N4Py)-Fe(III)-O_2]$^+$ (TMC = 1,4,8,11-tetramethyl-1,4,8,11-tetraazacyclotetradecane; N4Py = *N*,*N*-bis(2-pyridylmethyl)-*N*-

(5) Cryle, M. J.; Matovic, N. J.; De Voss, J. J. *Org. Lett.* **2003**, *5*, 3341.
(6) Umehara, K.; Kudo, S.; Hirao, Y.; Morita, S.; Uchida, M.; Odomi, M.; Miyamoto, G. *Drug Metab. Dispos.* **2000**, *28*, 887.
(7) Henry, K. M.; Townsend, C. A. *J. Am. Chem. Soc.* **2005**, *127*, 3724.
(8) Roberts, E. S.; Vaz, A. D.; Coon, M. J. *Proc. Natl. Acad. Sci. U.S.A.* **1991**, *88*, 8963.
(9) Akhtar, M.; Calder, M. R.; Corina, D. L.; Wright, J. N. *Biochem. J.* **1982**, *201*, 569.
(10) Vaz, A. D. N.; Roberts, E. A.; Coon, M. J. *J. Am. Chem. Soc.* **1991**, *113*, 5886.
(11) Shyadehi, A. Z.; Lamb, D. C.; Kelly, S. L.; Kelly, D. E.; Schunck, W. H.; Wright, J. N.; Corina, D.; Akhtar, M. *J. Biol. Chem.* **1996**, *271*, 12445.
(12) Cole, P. A.; Bean, J. M.; Robinson, C. H. *Proc. Natl. Acad. Sci. U.S.A.* **1990**, *87*, 2999.
(13) Fishman, J.; Raju, M. S. *J. Biol. Chem.* **1981**, *256*, 4472.
(14) Fishman, J. *Cancer Res.* **1982**, *42*, 3277s.
(15) Gupta, A. K.; Tomas, E. *Dermatol. Clin.* **2003**, *21*, 565.
(16) Meis, J. F.; Verweij, P. E. *Drugs* **2001**, *61*, S13.
(17) Zhou, W.; Lepesheva, G. I.; Waterman, M. R.; Nes, W. D. *J. Biol. Chem.* **2006**, *281*, 6290.
(18) Croft, S. L. *Parasite (Paris, France)* **2008**, *15*, 522.
(19) Lepesheva, G. I.; Waterman, M. R. *Mol. Cell. Endocrinol.* **2004**, *215*, 165.
(20) Lepesheva, G. I.; Hargrove, T. Y.; Kleshchenko, Y.; Nes, W. D.; Villalta, F.; Waterman, M. R. *Lipids* **2008**, *43*, 1117.
(21) Brueggemeier, R. W.; Hackett, J. C.; Diaz-Cruz, E. S. *Endocr. Rev.* **2005**, *26*, 331.
(22) Rugo, H. S. *Ann. Oncol.* **2008**, *19*, 16.
(23) Hackett, J. C.; Brueggemeier, R. W.; Hadad, C. M. *J. Am. Chem. Soc.* **2005**, *127*, 5224.
(24) Vaz, A. D.; Pernecky, S. J.; Raner, G. M.; Coon, M. J. *Proc. Natl. Acad. Sci. U.S.A.* **1996**, *93*, 4644.
(25) Selke, M.; Sisemore, M. F.; Ho, R. Y. N.; Wertz, D. L.; Valentine, J. S. *J. Mol. Catal. A: Chem.* **1997**, *117*, 71.
(26) Wertz, D. L.; Sisemore, M. F.; Selke, M.; Driscoll, J.; Valentine, J. S. *J. Am. Chem. Soc.* **1998**, *120*, 5331.
(27) Annaraj, J.; Suh, Y.; Seo, M. S.; Kim, S. O.; Nam, W. *Chem. Commun.* **2005**, 4529.
(28) Park, M. J.; Lee, J.; Suh, Y.; Kim, J.; Nam, W. *J. Am. Chem. Soc.* **2006**, *128*, 2630.

bis(2-pyridyl)methylamine) which deformylate 2-propionaldehyde to acetophenone.[27,28]

CYP51 from *Mycobacterium tuberculosis* is the first steroidogenic CYP catalyzing deformylation for which a high-resolution crystal structure is available.[29,30] This structure provides an unprecedented opportunity to study short-lived reactive oxygen intermediates and explore deformylation mechanisms using contemporary computational methods. Herein, we present the application of molecular dynamics (MD) simulation and hybrid quantum mechanics/molecular mechanics (QM/MM) methods to explore the role of reactive oxygen intermediates in a CYP-catalyzed deformylation. The results of these studies provide insight into the catalytic mechanisms of several biosynthetic and xenobiotic metabolizing CYPs of biomedical importance.

2. Methods

2.1. System Preparation and MD Simulation. MD simulations of CYP51 were performed as previously described[31] using NAMD 2.6[32] and the CHARMM27[33] force field. The propKa module of the PDB2PQR suite of programs[34−36] and visual inspection of local side chain environments were used to adjust the protonation states of ionizable residues. Unless otherwise noted, all acidic residues were deprotonated (negatively charged), while arginine and lysine residues were protonated (positively charged). Histidine residues were either doubly protonated (101, 113, 259, 392), singly protonated at N^{δ} (13, 16, 18, 57, 170, 258, 275, 337, 340, 363, 430), or singly protonated at N^{ε} (299, 318). Therefore, except in cases when Glu173 is protonated, the protein backbone has a charge of $-12e$. MM parameters for the iron protoporphyrin IX and O_2 were taken from the CHARMM22 force field.[33,37] MM parameters for Cmpd I were from Bathelt and co-workers.[38] The MM parameter set for lanosterol[39] was extended to include parameters for the carboxaldehyde and geminal diol units using (1*R*,6*S*,9*S*)-1,1-dimethylbicyclo[4.3.0]nonane-6-carboxaldehyde and the corresponding diol as truncated models, respectively. Additional parameters were generated from automated frequency matching[40] to B3LYP/6-31G(d) harmonic vibrational frequency analyses of fully optimized geometries. Dihedral parameters were derived from relaxed potential energy surface scans of 2,2-dimethylpropanal, and electrostatic potential charges were derived using the CHELPG scheme.[41] Additional CHARMM parameters for 3β-hydroxylanosta-8,24-diene-32-al and 3β-hydroxylanosta-8,24-diene-32,32-diol (Scheme 2) are listed in the Supporting Information.

2.2. Partitioning of QM and MM Systems. Coordinates of the CYP51 protein, associated ligands, and a 5 Å bounding water shell were extracted from MD trajectory points, resulting in systems of ~14 000 atoms for QM/MM treatment. These systems were subjected to 11 000 geometry optimization steps using the CHARMM package.[37] Unless otherwise noted, optimized systems were partitioned into a region for QM treatment containing the O_2-coordinated porphyrin, the cysteinate 394 side chain, and the substrate C/D rings. Propionate, methyl, and vinyl side chains of the heme as well as the carbon units beyond C20 of substrates were excluded. Atoms within 7 Å of the QM region remained unrestrained during QM/MM geometry optimizations, while the remaining atoms were frozen.

2.3. Hybrid QM/MM Calculations. QM/MM calculations were performed with the ChemShell[42] package, which integrates the TURBOMOLE[43] and DL-POLY[44] packages for density functional theory and MM calculations, respectively. The electrostatic embedding scheme with the charge shift correction was used to represent the electrostatic interaction between the QM region and the surrounding partial charge distribution.[45] In QM/MM geometry optimizations, the QM region was treated with the B3LYP[46−48] density functional and the Ahlrichs VTZ[49] for Fe, 6-31+G(d) for N, O, S and the 6-31G(d) basis sets for C, H. The CHARMM27[33] force field was used for the MM region. Stationary points were subject to single point calculations with the B3LYP and PBE0[50] density functionals, Wachter's +f basis set[51,52] for Fe, and TZVP[53] basis set for the remaining atoms. Basis sets for geometry optimizations and single-point energy calculations are denoted B1 and B2 in the text, respectively. Explicit Hessian matrices of transition states, generated by the finite difference scheme in ChemShell, were characterized by a single negative eigenvalue. Population analyses were performed with the natural population analysis method.[54]

3. Results and Discussion

3.1. MD Simulation. A prerequisite for exploration of the CYP51 deformylation mechanism is to sample catalytically competent orientations of the substrate. To this end, explicit solvent MD simulations were used to explore configurations of the 3β-hydroxylanosta-8,24-dien-32-al and 3β-hydroxylanosta-8,24-dien-32,32-diol intermediates and solvation of the CYP51 active site. In a previous theoretical study of proton transport pathways in this enzyme, extended MD simulations with the lanosterol substrate were performed.[31] A novel hydrogen-bonded network of water molecules was observed in the active site, which QM/MM calculations demonstrated could catalyze Cmpd I formation. Rather than starting with crystallographic coordinates as initial positions for this study, the lanosterol from the equilibrated simulation was replaced by these intermediates (Scheme 2) and the simulations were resumed.

To restrict sampling of 3β-hydroxylanosta-8,24-dien-32-al to catalytically competent orientations for the concerted deformylation reaction proposed by Shyadehi,[11] harmonic restraints (20 kcal·mol^{-1}·Å^{-1}) were applied between the C32 and distal O_2

(29) Podust, L. M.; Yermalitskaya, L. V.; Lepesheva, G. I.; Podust, V. N.; Dalmasso, E. A.; Waterman, M. R. *Structure* **2004**, *12*, 1937.
(30) Podust, L. M.; Poulos, T. L.; Waterman, M. R. *Proc. Natl. Acad. Sci. U.S.A.* **2001**, *98*, 3068.
(31) Sen, K.; Hackett, J. C. *J. Phys. Chem. B* **2009**, *113*, 8170.
(32) Phillips, J. C.; Braun, R.; Wang, W.; Gumbart, J.; Tajkhorshid, E.; Villa, E.; Chipot, C.; Skeel, R. D.; Kale, L.; Schulten, K. *J. Comput. Chem.* **2005**, *26*, 1781.
(33) MacKerell, A. D.; et al. *J. Phys. Chem. B* **1998**, *102*, 3586.
(34) Bas, D. C.; Rogers, D. M.; Jensen, J. H. *Proteins* **2008**, *73*, 765.
(35) Dolinsky, T. J.; Czodrowski, P.; Li, H.; Nielsen, J. E.; Jensen, J. H.; Klebe, G.; Baker, N. A. *Nucleic Acids Res.* **2007**, *35*, W522.
(36) Kieseritzky, G.; Knapp, E. W. *J. Comput. Chem.* **2008**, *29*, 2575.
(37) Brooks, B. R.; Bruccoleri, R. E.; Olafson, B. D.; States, D. J.; Swaminathan, S.; Karplus, M. *J. Comput. Chem.* **1983**, *4*, 187.
(38) Bathelt, C. M.; Zurek, J.; Mulholland, A. J.; Harvey, J. N. *J. Am. Chem. Soc.* **2005**, *127*, 12900.
(39) Cournia, Z.; Smith, J. C.; Ullmann, G. M. *J. Comput. Chem.* **2005**, *26*, 1383.
(40) Vaiana, A. C.; Cournia, Z.; Costescu, I. B.; Smith, J. C. *Comput. Phys. Commun.* **2005**, *167*, 34.
(41) Breneman, C. M.; Wiberg, K. B. *J. Comput. Chem.* **1990**, *11*, 361.
(42) Sherwood, P.; et al. *J. Mol. Struct.* **2003**, *632*, 1.
(43) Ahlrichs, R.; Bär, M.; Häser, M.; Horn, H.; Kölmel, C. *Chem. Phys. Lett.* **1989**, *162*, 165.
(44) Smith, W.; Forester, T. R. *J. Mol. Graphics* **1996**, *14*, 136.
(45) Bakowies, D.; Thiel, W. *J. Phys. Chem.* **1996**, *100*, 10580.
(46) Lee, C.; Yang, W.; Parr, R. G. *Phys. Rev. B* **1988**, *37*, 785.
(47) Becke, A. D. *J. Chem. Phys.* **1993**, *98*, 1372.
(48) Becke, A. D. *Phys. Rev. A* **1988**, *38*, 3098.
(49) Schäfer, A.; Horn, H.; Ahlrichs, R. *J. Chem. Phys.* **1992**, *97*, 2571.
(50) Perdew, J. P.; Ernzerhof, M.; Burke, K. *J. Chem. Phys.* **1996**, *105*, 9982.
(51) Bauschlicher, C. W., Jr.; Langhoff, S. R.; Partridge, H.; Barnes, L. A. *J. Chem. Phys.* **1989**, *91*, 2399.
(52) Wachters, A. J. H. *J. Chem. Phys.* **1970**, *52*, 1033.
(53) Schäfer, A.; Huber, C.; Ahlrichs, R. *J. Chem. Phys.* **1994**, *100*, 5829.
(54) Reed, A. E.; Weinstock, R. B.; Weinhold, F. *J. Chem. Phys.* **1985**, *83*, 735.

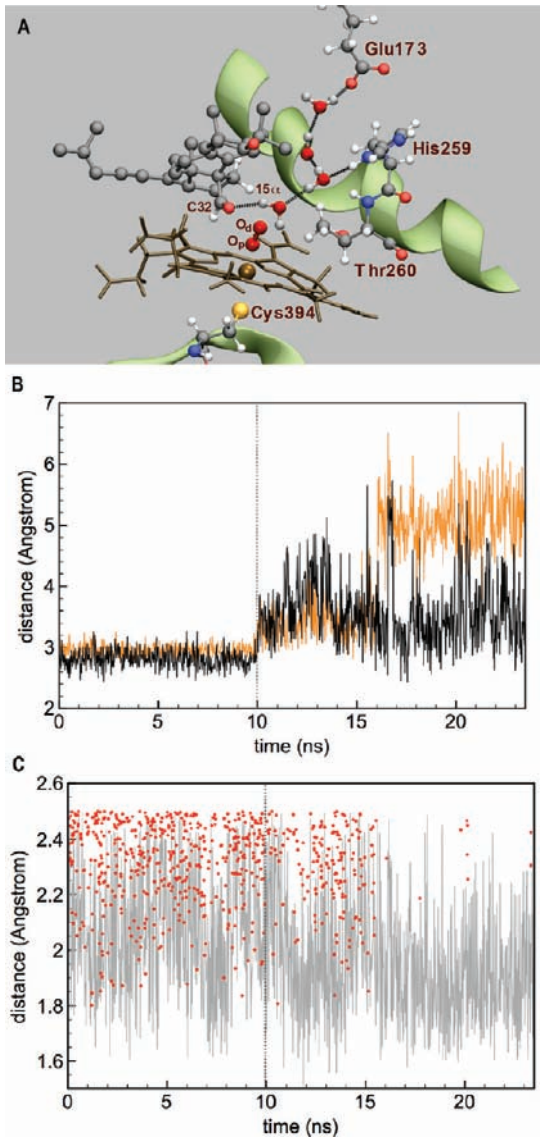

Figure 1. MD simulation of the CYP51-3β-hydroxylanosta-8,24-diene-32-al complex. (A) Active site configuration of a representative molecular dynamics trajectory point used for QM/MM studies of the peroxo-mediated deformylation of 3β-hydroxylanosta-8,24-diene-32-al. Selected hydrogen atoms are removed from the substrate for clarity. (B) Distal O_2−C32 (orange) and 15αH-proximal O_2 (black) distances. (C) Carboxaldehyde O−H_2O (gray) hydrogen bond distances. Establishment of a hydrogen bond between the water network and distal O_2 atom, as defined by an encounter distance of less than 2.5 Å, is recorded as red circles. Dotted lines indicate the time point when the harmonic restraints are released.

atoms, as well as between the 15α-hydrogen atom and proximal O_2 atoms. A representative orientation of 3β-hydroxylanosta-8,24-dien-32-al in the CYP51 active site is shown in Figure 1A. Over the 10 ns of restrained NPT production simulation the distances between these atoms are stable, with average pairwise values of 3.0 ± 0.1 and 2.8 ± 0.1 Å, respectively (Figure 1B). The previously observed water network connecting Glu173 to the catalytic core (Figure 1A) is established in the presence of the harmonic restraints; however, the 3β-hydroxylanosta-8,24-dien-32-al carboxaldehyde is the terminal hydrogen bond acceptor in 75% of frames rather than O_2 or Thr260. In the first 10 ns, carboxaldehyde−water hydrogen bonding is stable, with an average hydrogen bond distance of 2.0 ± 0.2 Å (Figure 1C). Beyond 10 ns, the harmonic restraints between the carboxaldehyde substrate and O_2 were removed and the simulation was continued for an additional 13.5 ns. In these frames, the average distance between the carboxaldehyde and O_2 does increase to 3.4 ± 0.3 Å over 10−16 ns and to 5.1 ± 0.5 Å over 16−23.5 ns (Figure 1B). Nevertheless, in the unrestrained simulation, the average carboxaldehyde−water hydrogen bond remains 1.9 ± 0.2 Å. Furthermore, as illustrated in Figure 1C, the frequency with which the terminal water molecule contributes a hydrogen bond to the O_2 distal oxygen atom (as defined by an approach within 2.5 Å) decreases. However, in the latter 13.5 ns, the water network terminates with the carboxaldehyde in over 90% of frames. This indicates that even without harmonic restraints between the substrate and O_2, establishment of the putative proton transfer network to O_2 is a relatively rare event in these MD simulations. In contrast to the lanosterol substrate, the 32-carboxaldehyde likely diverts the proton shuttle from the distal O_2 atom to the aldehyde. Disruption of the proton relay network by the aldehyde substrate would provide an opportunity for the peroxo intermediate to participate in catalysis.

On the basis of these observations, it is also reasonable to predict that diversion of the proton transfer network may occur in the second step of CYP51 catalysis. It is generally accepted that this step is a Cmpd I mediated hydroxylation of 3β-hydroxylanosta-8,24-dien-32-ol. The MD results obtained with the aldehyde indicate that this hydroxylated intermediate could similarly divert the hydrogen-bonded network of water away from the peroxo distal O_2 atom. Although this aspect is beyond the scope of the current study which is focused on the final catalytic step, this situation may provide an opportunity for participation of the C32 hydroxyl to assist proton transfer by intervening in the hydrogen bond network, thereby acting as a conduit for proton transfer to peroxo and compound **0** (Cmpd 0). Substrate-assisted O_2 activation has been proposed in other CYP-catalyzed reactions. One example is illustrated in the recent crystal structure of Fe^{2+}-O_2 CYP107A that reveals that the 5-OH of deoxyerythronolide B apparently donates a hydrogen bond to O_2 and participates in the proton shuttle.[55]

Previous density functional theory studies with truncated models of the CYP active site and the aromatase geminal diol catalytic intermediate indicated that Cmpd I could perform the deformylation reaction.[23] The prerequisite MD simulations of 3β-hydroxylanosta-8,24-dien-32,32-diol (Scheme 2) bound to CYP51 Cmpd I were performed to evaluate these mechanisms utilizing the QM/MM approach (*vide infra*). A representative orientation of 3β-hydroxylanosta-8,24-dien-32,32-diol in the CYP51 active site is shown in Figure 2A. A single harmonic restraint (20 kcal·mol^{-1}·Å^{-1}) was applied between the Cmpd I oxygen and C15 atoms to maintain the diol in a competent orientation for study of deformylation initiated by the previously described hydrogen-atom abstraction, proton-coupled electron transfer mechanism.[23] Over the 10 ns simulation, the average distance between the 15α-hydrogen and Cmpd I oxygen atoms is 2.5 ± 0.1 Å (see Supporting Information). The geminal hydroxyl groups contribute hydrogen bonds to the Cmpd I oxygen with nearly equal frequency, and the average hydrogen bond distance is 2.1 ± 0.2 Å (Figure 2B). Two water molecules connect Glu173 to the Thr260 hydroxyl, while a third molecule is oriented between the Thr260 hydroxyl group and the Cmpd I oxygen, thus completing the hydrogen bond network between the geminal-diol and Glu173. (Figure 2A) Hydrogen-bonding

(55) Nagano, S.; Cupp-Vickery, J. R.; Poulos, T. L. *J. Biol. Chem.* **2005**, *280*, 22102.

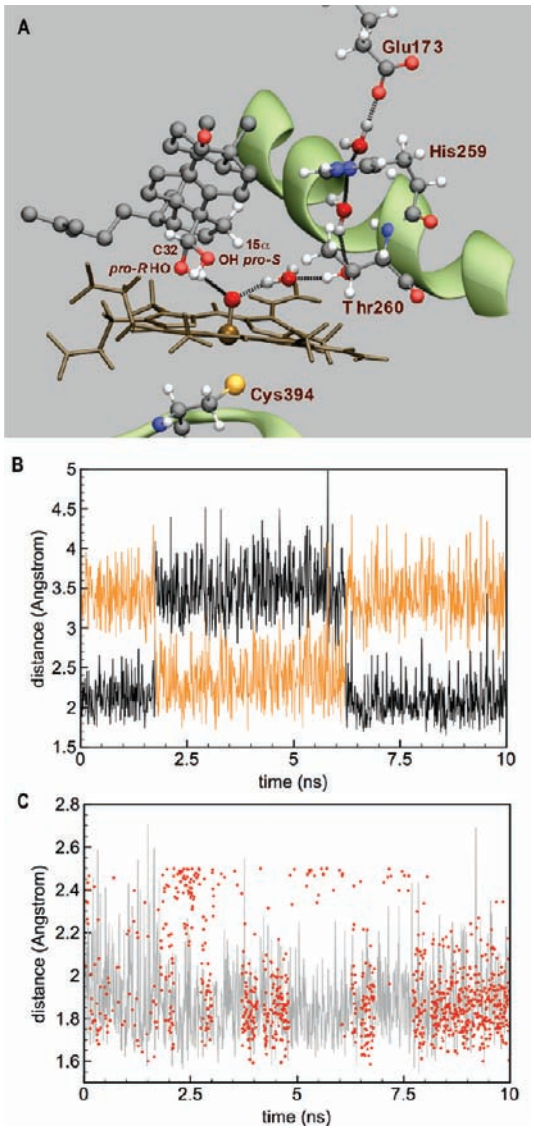

Figure 2. MD simulation of the CYP51-3β-hydroxylanosta-8,24-diene-32,32-diol complex. (A) Active site configuration of a representative molecular dynamics trajectory point used for QM/MM studies of the Cmpd I mediated deformylation of 3β-hydroxylanosta-8,24-diene-32,32-diol. Selected hydrogen atoms are removed from the substrate for clarity. (B) Hydrogen bond distance between the substrate *pro-R* (black) and *pro-S* (orange) hydroxyl groups and Cmpd I oxygen. (C) Distances between the Cmpd I oxygen$-H_2O$ (gray). Establishment of a hydrogen bond between the Thr260 hydroxyl and bridging water molecule, as defined by an encounter distance of less than 2.5 Å, is recorded as red circles.

to Cmpd I by this intervening water molecule is stable over the trajectory with an average distance of 1.9 ± 0.2 Å. However, its hydrogen bond to the Thr260 hydroxyl is transient, forming an apparent hydrogen bond in only half of the MD trajectory points with an average hydrogen bond distance of 1.9 ± 0.2 Å. The time evolution of these distances over the MD trajectory are reported in Figure 2C.

3.2. Hybrid QM/MM Calculations. Peroxo intermediates of heme- and non-heme organoiron complexes have been shown to deformylate aldehydes,[25−28] and CYP mechanistic studies using isotopically labeled substrates are consistent with participation of the peroxo species.[8−11,24] Nonetheless, in contrast to the number of mechanistic studies of CYPs catalyzing hydroxylation, those catalyzing aldehyde deformylation have received less attention. Electron paramagnetic resonance (EPR) experiments and theoretical studies of CYP101, which catalyzes hydroxylation of camphor, indicate protonation of peroxo proceeds with a low energetic barrier.[56,57] In contrast, the CYP19 peroxo intermediate was cryotrapped and upon gradual cryoannealing was stable to ∼180 K. Furthermore, there was no evidence for accumulation of the hydroperoxo species in CYP19, indicating that the proton transfer network in this enzyme is more hindered relative to CYP101.[58] Despite differences in the active site architecture of these enzymes compared to CYP51, this study confirms that the active sites of CYP enzymes modulate the lifetimes of reactive oxygen species differently. Moreover, the direct characterization of the peroxo intermediate indicates that this species cannot be discounted as a viable oxidant in CYP-catalyzed reactions. We hypothesize that features of the aldehyde substrate and CYP51 active site are necessary to divert the proton transfer network from the peroxo oxygen atoms, thus affording a lifetime sufficient for peroxo to undergo nucleophilic addition and hence function as a competent catalytic intermediate. Diversion of the Glu173 initiated proton transfer network in MD simulations of the lanosterol carboxaldehyde/CYP51 system supports this hypothesis. Nonetheless, given the limitations of MD simulation to sample hydrogen bond networks which could afford alternative reactive oxygen intermediates, deformylation mechanisms mediated by the peroxo, Cmpd 0, and Cmpd I were evaluated with the QM/MM approach. Unless otherwise noted, QM/MM energies and population analyses reported in the subsequent discussion are at the B3LYP/B1:CHARMM and B3LYP/B2//B1:CHARMM levels of theory, respectively. A complete list of energies and spin densities for each species and theoretical levels applied herein can be found in the Supporting Information.

3.2.1. Nucleophilic Addition of the Peroxo and Compound 0 Intermediates. To explore the energetics of nucleophilic addition of the peroxo intermediate, potential energy surfaces for addition of the distal O_2 atom to the aldehyde carbon were mapped with the QM/MM method using QM systems of various sizes (Figure 3). Potential energy surfaces were restricted to the doublet spin state, in accordance with EPR studies[59] and previous QM/MM[60] studies of this intermediate. Our laboratory previously demonstrated that when Glu173 is protonated, an oxyferrous species with a Glu173-centered radical anion, isoelectronic with the peroxo intermediate, is observed.[31] EPR studies of the peroxo intermediate in other CYP enzymes, including CYP19 which is known to cleave C−C bonds, are not consistent with this spin-delocalized electronic structure. Comparison of the recent crystal structure of human placental CYP19[61] illustrates that a corresponding acidic residue is not structurally conserved. Moreover, structural comparisons of CYP51[29] with CYP101[62] indicate that Asp182 is similarly oriented in the active site; however, the propKa pK_a estimate for this residue is 2.7, thereby largely precluding its protonation

(56) Wang, D.; Zheng, J.; Shaik, S.; Thiel, W. *J. Phys. Chem. B* **2008**, *112*, 5126.
(57) Davydov, R.; Makris, T. M.; Kofman, V.; Werst, D. E.; Sligar, S. G.; Hoffman, B. M. *J. Am. Chem. Soc.* **2001**, *123*, 1403.
(58) Gantt, S. L.; Denisov, I. G.; Grinkova, Y. V.; Sligar, S. G. *Biochem. Biophys. Res. Commun.* **2009**, *387*, 169.
(59) Davydov, R.; Kappl, R.; Hüttermann, J.; Peterson, J. A. *FEBS Lett.* **1991**, *295*, 113.
(60) Wang, D.; Thiel, W. *J. Mol. Struct.* **2009**, *898*, 90.
(61) Ghosh, D.; Griswold, J.; Erman, M.; Pangborn, W. *Nature* **2009**, *457*, 219.
(62) Schlichting, I.; Berendzen, J.; Chu, K.; Stock, A. M.; Maves, S. A.; Benson, D. E.; Sweet, R. M.; Ringe, D.; Petsko, G. A.; Sligar, S. G. *Science* **2000**, *287*, 1615.

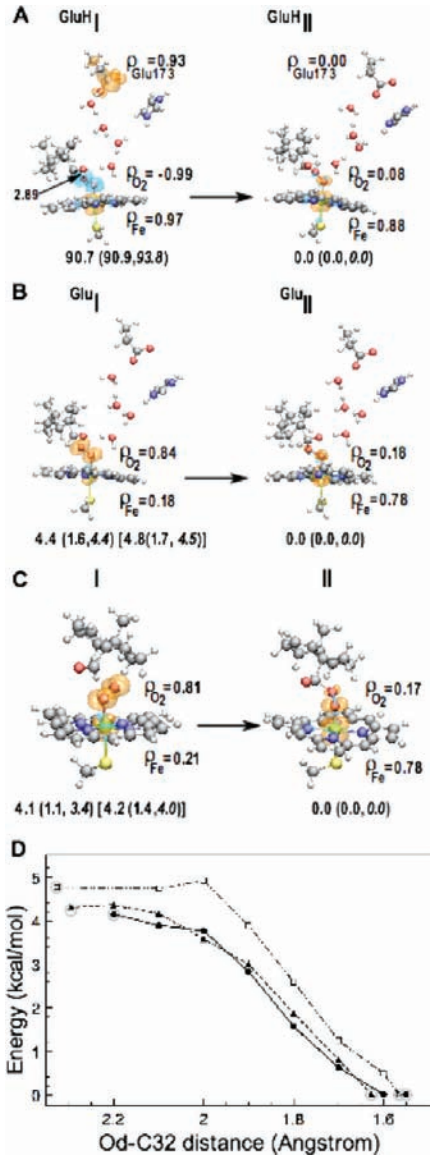

Figure 3. (A) B3LYP/B1:CHARMM geometries of the oxyferrous/glutamyl radical anion (^{GluH}**I**) and protonated peroxohemiacetal (^{GluH}**II**) with the complete proton transfer network included in the QM region. (B) B3LYP/B1:CHARMM geometries of the peroxo intermediate (^{Glu}**I**) and deprotonated peroxohemiacetal (^{Glu}**II**) with the complete proton transfer network included in the QM region. Relative QM/MM energies when water is partitioned in the MM region are listed in square brackets. (C) B3LYP/B1:CHARMM geometries of the peroxo intermediate (**I**) and deprotonated peroxohemiacetal (**II**) with the complete proton transfer network included in the MM region. QM/MM energies derived from a second MD frame are listed in square brackets. (D) B3LYP/B1:CHARMM surfaces for peroxo nucleophilic addition. Nucleophilic addition in ^{Glu}**I** less the intervening water molecules are represented by □. Nucleophilic addition surfaces for **I** from two MD configurations are represented by ▲ and ●. Data points corresponding to unrestrained, fully optimized geometries are represented with gray circles. Single-point B3LYP/B2//B1:CHARMM and PBE0/B2//B3LYP/B1:CHARMM (italicized) energies are in parentheses. Energies are relative to the peroxohemiacetal intermediates. Spin difference density surfaces are plotted with isocontour values of ±0.002 au.

at physiological pH. Thus, it is not surprising that the peroxo intermediates of these enzymes do not exhibit spectra characteristic of an amino acid centered radical.[57,58] To determine whether this electronic structure persists with 3β-hydroxylanosta-8,24-dien-32-al in the active site and to study the influence of the Glu173 protonation state on peroxo nucleophilicity, the Glu173 and His259 side chains as well as the intervening water molecules were included in the QM region (Figure 3A, ^{GluH}**I**). When Glu173 is protonated, an oxyferrous/Glu173 radical anion species is observed similar to when lanosterol is present in the active site.[31] As illustrated by the spin difference density contour plots and NPA spin densities, the system is triradicaloid with two electrons of antiparallel spin localized to the Fe and O_2 units, while the third electron is localized to the protonated Glu173 side chain (Figure 3A, ^{GluH}**I**). The reaction coordinate, defined as the distance between the distal O_2 atom and the aldehyde carbon, was then varied stepwise and the corresponding energy calculated using the QM/MM methodology. This oxyferrous/glutamyl radical anion configuration could be optimized to an apparently stable intermediate on the potential energy surface. However, attempts to perform restrained optimizations along several points of the nucleophilic reaction coordinate resulted in spontaneous proton flow from the Glu173 side chain to the aldehyde oxygen. This occurred concomitantly with electron transfer from protonated Glu173 to the oxyferrous unit. Together, they result in a protonated peroxohemiacetal species 90.7 kcal/mol below the corresponding prereactant complex (Figure 3A, ^{GluH}**I** → ^{GluH}**II**). To maintain consistency with the remainder of the discussion, energies reported in Figure 3 are relative to the peroxohemiacetal species. Therefore, despite diversion of the putative proton relay from O_2, the hydrogen-bonded network remains functional to protonate the impending aldehyde oxyanion of the peroxohemiacetal. As predicted from propKa calculations, the elevated pK_a of Glu173 (8.3), taken together with its access to the solvent, strengthens the argument for its role in proton transport.[31]

Conversely, when Glu173 is deprotonated, no delocalization occurs and the peroxo has an electronic structure similar to those previously reported in the QM/MM studies of CYP101[60] (Figure 3B, ^{Glu}**I**). Nevertheless, we attempted to map the reaction coordinate with deprotonated Glu173 and the intervening water molecules (Figure 3B, ^{Glu}**I** → ^{Glu}**II**); however, as in Figure 3A (^{GluH}**I** → ^{GluH}**II**), the large QM system resulted in a rugged potential energy surface that was difficult to interpret. However, full geometry optimization revealed formation of the unprotonated peroxohemiacetal to be 4.4 kcal/mol exothermic (Figure 3B, ^{Glu}**I** → ^{Glu}**II**). To make construction of the potential energy surface more tractable, the intervening water molecules were partitioned into the MM region. This QM system afforded the smooth potential energy surface illustrated in Figure 3D. In this partitioning scheme, the peroxo intermediate is apparently a stable intermediate. However, the potential energy surface in the vicinity of this species is relatively flat and does not provide clear evidence of a energetic barrier for nucleophilic addition (Figure 3D). Thus, with the intervening waters in the MM layer, peroxo undergoes nucleophilic addition without an apparent energetic barrier to form the unprotonated peroxohemiacetal with an exothermicity of 4.8 kcal/mol. In either case, these results support that formation of the peroxohemiacetal is feasible regardless of the Glu173 protonation state and therefore could offer a branch point in the catalytic mechanism leading to deformylation.

The deprotonated peroxohemiacetal (Figure 3B, ^{Glu}**II**) does not delocalize an electron to the Glu173 side chain. To verify if Glu173 is a spectator of peroxo addition when deprotonated and to determine whether its presence influences the electronic structure of the peroxohemiacetal, the potential energy surfaces for peroxo addition were calculated with Glu173 and His259 treated at the MM level of theory (Figure 3C, **I** → **II**). To ensure that the result was not an artifact of a single MD trajectory point,

two geometries separated by 1.7 ns in the MD simulation were selected. Potential energy surfaces for peroxo addition in each of these configurations are shown in Figure 3D. When the deprotonated Glu173 is present in the MM region, the potential energy surface is relatively flat in the vicinity of this species. Furthermore, these surfaces indicate that nucleophilic addition is apparently barrierless and results in the formation of a peroxohemiacetal species 4.1−4.2 kcal/mol below the peroxoheme/3β-hydroxylanosta-8,24-dien-32-al complex (Figure 3C, **I** → **II**). Since these results suggest that the protonation state of Glu173 does not influence the electronic structure of the peroxohemiacetal and moreover would make transition state identification for reactive processes difficult, unless otherwise noted, Glu173, His259 atoms, and intervening water molecules were partitioned into the MM region for the remaining calculations.

It has been proposed that the Cmpd 0 intermediate can behave as a nucleophile and attack the carbonyl group of an aldehyde during CYP-catalyzed deformylation.[11,63] In an effort to investigate a role for this intermediate, QM/MM potential energy surfaces were constructed for nucleophilic addition of Cmpd 0 to the carboxaldehyde. A transition state for addition of the distal O_2 atom of Cmpd 0 was identified and, with decreased nucleophilicity, proceeds with an energetic barrier of 23.8 kcal/mol. Consistent with a late transition state, the O−O bond is essentially broken (2.00 Å) and the Fe−O bond is shortened by 0.18 Å. This transition state geometry indicates that this reaction is more akin to homolytic O−O cleavage and addition of a hydroxyl radical ($\rho^{OH} = -0.32$, $q^{OH} = -0.07$) to the aldehyde. Optimization of the transition state leads to nearly thermoneutral formation of an oxyradical intermediate and compound **II** (Cmpd II) species, 1.5 kcal/mol below the Cmpd 0/3β-hydroxylanosta-8,24-dien-32-al complex. The QM/MM transition state and intermediates for the Cmpd 0 addition are reported in the Supporting Information. In accord with this theoretical prediction, Park and co-workers generated several hydroperoxo non-heme ferric complexes that are unable to deformylate 2-phenylpropionaldehyde.[28] In a recent study of Cmpd I formation in CYP51, the barrier for protonation of Cmpd 0 to form Cmpd I was calculated to be at least 12 kcal/mol.[31] Taken together with the relatively high barrier for Cmpd 0 addition to the aldehyde, it is unlikely that this intermediate significantly contributes to deformylation. Thus, if Cmpd 0 is formed, even in the presence of the aldehyde substrate, the catalytic cycle is dedicated to Cmpd I formation or uncoupling to H_2O_2.

3.2.2. Deformylation from the Deprotonated Peroxohemiacetal. First, stepwise deformylation mechanisms starting from the deprotonated peroxohemiacetal (Figures 3 and 4, **II**) are considered. In search of transition states, potential energy surfaces for both the C14−C32 and O−O reaction coordinates were explored. The potential energy surface for C14−C32 cleavage is relatively flat, rendering efforts using this coordinate to identify an authentic transition state unsuccessful. From estimation of the barrier from the highest point on the potential energy surface, the C14−C32 bond breaks with an apparent barrier of 0.8 kcal/mol. This approximate transition state (Figure 4, $\mathbf{IV}^{\ddagger}$) was successfully connected to the peroxohemiacetal intermediate as well as a peroxoformate/deformylated substrate complex (Figure 4, **V**) 17.3 kcal/mol exothermic relative to the peroxohemiacetal. Natural population analysis of this intermediate complex revealed a group charge of $q = -0.76$ and spin density of $\rho = 0.23$ on the deformylated substrate. This indicates that the deformylated substrate is more akin to an allylic carbanion, and therefore, the C−C bond cleavage reaction is best described as heterolytic. For comparison, the transition state for C−C cleavage of the peroxohemiacetal in a truncated model was identified and connected to these intermediates in the gas phase. Optimized geometries for the gas phase transition state and intermediates for C−C cleavage are reported in the Supporting Information. In the absence of the protein environment, the deformylated substrate accumulates nearly a single electron ($\rho = 0.84$) and minimal charge ($q = -0.17$) consistent with homolytic cleavage of the C−C bond. These differences suggest that the enzyme environment tunes the electronic structure of this intermediate, affecting the mechanism of bond cleavage.

Several additional calculations were performed to identify the active site environmental factor(s) contributing to the disparity in C−C cleavage mechanisms. The transition state C−C bond lengths are similar in the gas-phase and active site environments; however, the former lies 4.2 kcal/mol above the peroxohemiacetal, suggesting that the active site environment imparts minor stabilization of the transition state. Formation of peroxoformate is similarly exothermic in the gas phase, lying 18.3 kcal/mol below the peroxohemiacetal. Since the charge-separated character is greatest in the peroxoformate/deformylated substrate complex (Figure 4, **V**), this species was used to probe important environmental factors. The most notable geometric difference between these environments is the porphyrin geometry. The enzyme active site imparts geometric restraints on atoms in the QM region, distorting the porphyrin into a pseudoumbrella conformation, whereas in the gas phase it is planar. QM atoms containing the distorted porphyrin conformation from the QM/MM system were extracted into the gas phase, followed by recomputation of the density and population analyses, remaining characteristic of homolytic cleavage. These results indicate that the origin of the heterolytic cleavage is not geometric distortion of the catalytic core by the active site but rather electrostatic interactions contributed by the enzyme environment. Histidinium 259 localizes positive charge adjacent to the deformylated substrate, possibly stabilizing the carbanion intermediate (Figure 1A). However, after deletion of this residue's contribution to the partial charge distribution, the deformylated substrate still resembles a carbanion. The results of peroxoformate environmental analyses are listed in Table 1.

Recently, analyses of the electric field environments at Fe and its ligand atoms were compared among CYP101, chloroperoxidase (CPO), and nitric oxide synthase (NOS) Cmpd I.[64] In CYP101 and CPO, the electric field vectors are roughly perpendicular to the heme, whereas the electric field vector of NOS is parallel to the heme plane. Coincidentally, the peroxo intermediate has also been implicated in NOS catalyzed conversion of N^G-hydroxy-L-arginine to citrulline.[65] This analysis has provided interesting insight into the nature of the electric field in the vicinity of Cmpd I and highlighted differences in the local electric field among these heme proteins. However, since the description provided by this analysis is localized, it provides little additional insight into the peroxoformate inter-

(63) Akhtar, M.; Corina, D.; Miller, S.; Shyadehi, A. Z.; Wright, J. N. *Biochemistry* **1994**, *33*, 4410.

(64) Cho, K. B.; Hirao, H.; Chen, H.; Carvajal, M. A.; Cohen, S.; Derat, E.; Thiel, W.; Shaik, S. *J. Phys. Chem. A* **2008**, *112*, 13128.

(65) Woodward, J. J.; Chang, M. M.; Martin, N. I.; Marletta, M. A. *J. Am. Chem. Soc.* **2009**, *131*, 297.

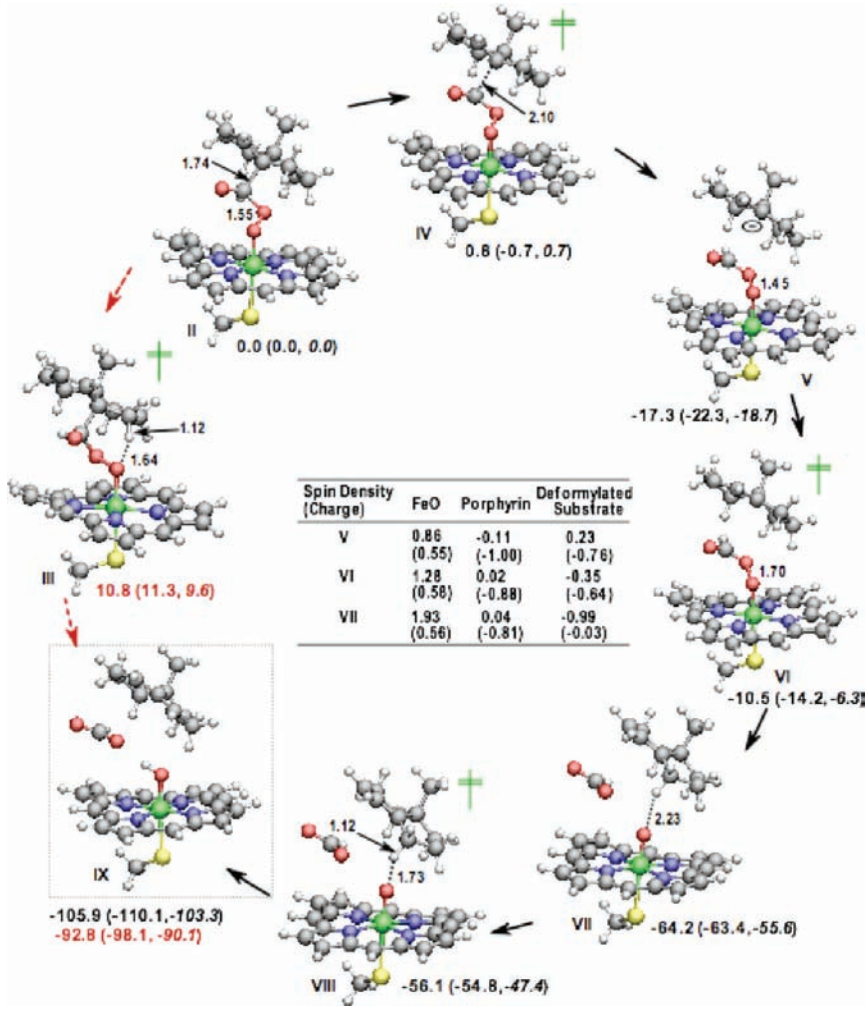

Figure 4. B3LYP/B1:CHARMM mechanisms for concerted (red, dotted arrows) and stepwise (black arrows) deformylation of the peroxohemiacetal intermediate. Single-point B3LYP/B2//B1:CHARMM and PBE0/B2//B3LYP/B1:CHARMM (italicized) energies are in parentheses. Energies (kcal/mol) are relative to the peroxohemiacetal species (**II**). Spin densities (charges) are derived from the B3LYP/B2//B1:CHARMM wave functions. Bond distances are in Å.

Table 1. NPA Spin Densities (Charges) for the Peroxoformate Intermediate (Figure 4, **V**) in Different Environmental Conditions

system	FeO	porphyrin	deformylated substrate
QM/MM	0.86 (0.55)	−0.11 (−1.00)	0.23 (−0.76)
QM/MM; His259 point charges deleted from MM region	0.82 (0.54)	−0.14 (−1.05)	0.31 (−0.68)
QM/MM geometry (gas phase)	0.87 (0.48)	−0.54 (−1.51)	0.65 (−0.35)
gas phase geometry[a]	0.88 (0.44)	−0.73 (−1.66)	0.84 (−0.17)

[a] In Supporting Information.

mediate, since the charges are spread over larger distances. Nonetheless, these results indicate a role for electrostatic effects in tuning the reactivities and altering the mechanisms of a number of CYP-catalyzed reactions.

In Figure 1A, two water molecules bridge the carboxaldehyde to histidinium 259, suggesting that if the peroxohemiacetal is sufficiently basic, the histidinium proton could be transferred via these water molecules to the peroxohemiacetal oxyanion and this protonated species could proceed through the remainder of CYP51 catalysis. These water molecules and the imidazolium side chain of His259 were included in the QM region to study protonation of the peroxohemiacetal and further investigate whether QM treatment of electrostatic contributions from this residue influence the energetics of C−C cleavage. A relaxed potential energy surface scan of the distance between the terminal water proton and peroxohemiacetal oxyanion, illustrated in the Supporting Information, smoothly increased to 13.2 kcal/mol, which corresponds to an O−H distance of 1.0 Å. Concerted reprotonation of the resulting hydroxide anion by histidinium does not occur, and release of the restraint returns to the unprotonated peroxohemiacetal complex. In view of the apparent improbability of proton transfer from histidinium to the peroxohemiacetal, the influence of electrostatic effects and hydrogen bonding on the energetics of C−C bond cleavage was reevaluated with the histidinium side chain and water molecules present in the QM region. The QM/MM potential energy surface for C−C bond cleavage is illustrated in Figure 5. Similar to the smaller QM representation of the active site, the potential energy surface for C−C cleavage is relatively flat, preventing efforts to identify a transition state. Nonetheless, C−C cleavage proceeds with an estimated 1.7 kcal/mol energetic barrier and the peroxoformate species lies 11.8 kcal/mol below the per-

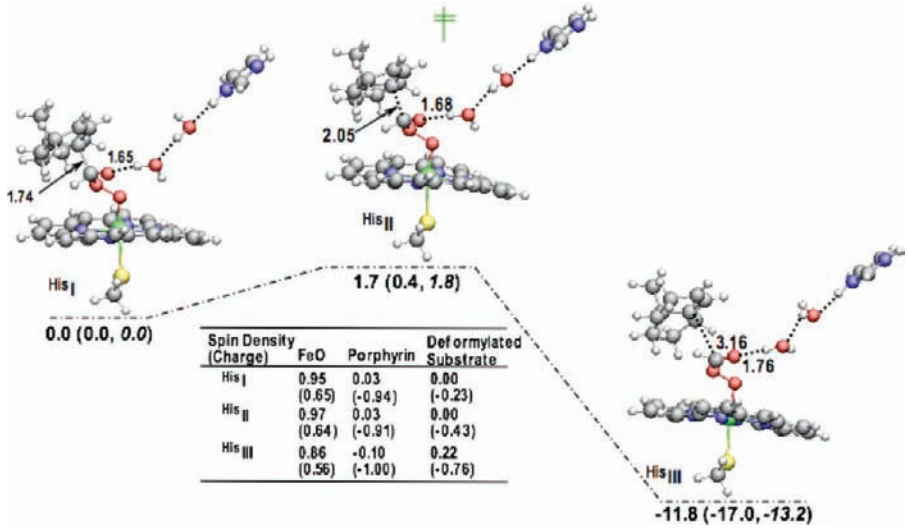

Figure 5. B3LYP/B1:CHARMM intermediates and transition state for peroxohemiacetal with the His259 imidazolium and bridging water molecules in the QM region. Single-point B3LYP/B2//B1:CHARMM and PBE0/B2//B3LYP/B1:CHARMM (italicized) energies are in parentheses. Energies (kcal/mol) are relative to the peroxohemiacetal species. Spin densities (charges) are derived from the B3LYP/B2//B1:CHARMM wave functions. Bond distances are in Å.

oxohemiacetal. Hence, results obtained with this expanded QM region confirm the earlier results obtained with a smaller QM representation. In the approximate transition state (Figure 5, ^{His}**II**‡), no spin density ($\rho = 0.00$) accumulates on the steroid fragment, and the corresponding charge is $q = -0.43$. Moreover, the charge ($q = -0.76$) and spin density ($\rho = 0.22$) of the steroid fragment in the peroxoformate product (Figure 5, ^{His}**III**) are also akin to an allylic carbanion. These results support that QM treatment of direct hydrogen bond interactions and electrostatic effects from these species does not significantly contribute to the C−C cleavage energetics or properties of the intermediates. Hence, these have been excluded from the QM region for the remainder of the mechanistic investigation.

An alternative fragmentation pathway for the peroxohemiacetal intermediate was explored, with the O−O bond distance defined as the reaction coordinate. By use of the highest point on the potential energy surface to initiate the transition state search, a second order saddle point was identified, 16.2 kcal/mol above the peroxohemiacetal intermediate at the B3LYP/B1 level of theory. The normal modes corresponding to the imaginary vibrational frequencies are associated with simultaneous cleavage of the O−O and C−C bonds as well as C−C bond cleavage alone. The second order saddle point was optimized to a transition state characterized by an imaginary frequency with a normal mode identifying this as the C−C bond cleavage transition state. A transition state for O−O cleavage could not be found. Nevertheless, the approximate energetics of such a transition state would render this reaction path uncompetitive in light of the negligible barrier identified for C−C cleavage.

To account for experimental observation of formate, the potential energy surface for decomposition of peroxoformate was investigated. The transition state (Figure 4, **VI**‡) for O−O bond cleavage was characterized and lies 6.8 kcal/mol above the peroxoformate intermediate, while expulsion of formate is 46.9 kcal/mol exothermic (Figure 4, **VII**). After cleavage of the O−O bond, the deformylated substrate is no longer a carbanion; rather, the absolute spin density increases to nearly unity ($\rho = -0.99$) and is neutral ($q = -0.03$). To be consistent with the formation of a neutral radical, these results suggest

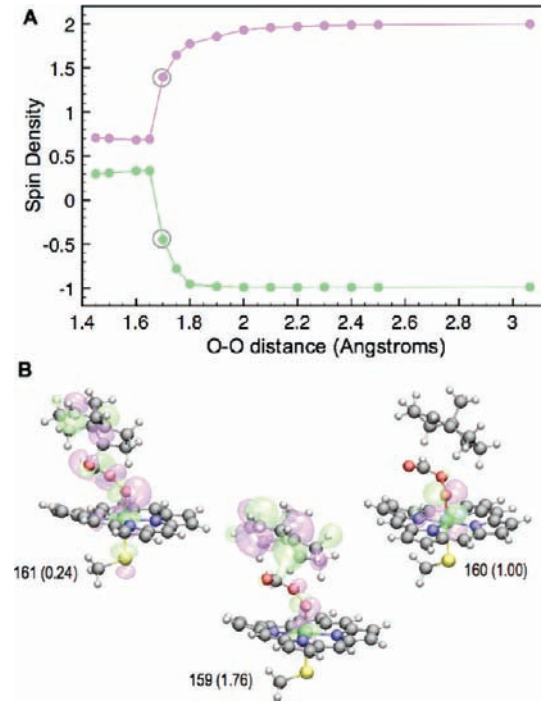

Figure 6. (A) B3LYP/B1:CHARMM group spin densities for the deformylated substrate (green) and [(porphyrin)(SCH_3)(FeO)] unit (magenta) along the reaction coordinate. Values for the transition state are highlighted with gray circles. (B) Frontier natural orbitals and occupation numbers (parentheses) of the peroxoformate O−O cleavage transition state. Natural orbital surfaces are plotted with isocontour values of ±0.02 au.

that an electron is transferred from the carbanion substrate in concert with O−O bond cleavage. Furthermore, the resulting iron−oxo species is characterized by two electrons of parallel spin localized to the Fe and O atoms ($\rho^{FeO} = 1.93$) and by a closed-shell porphyrin ($\rho^{Porphyrin} = 0.04$), characteristic of Cmpd II. Electron transfer along the O−O reaction coordinate is illustrated in Figure 6A. As the O−O bond lengthens, the spin density of the atoms of the forming iron−oxo species approaches 2, while a single electron of antiparallel spin accumulates on the deformylated substrate. The singly occupied natural orbitals

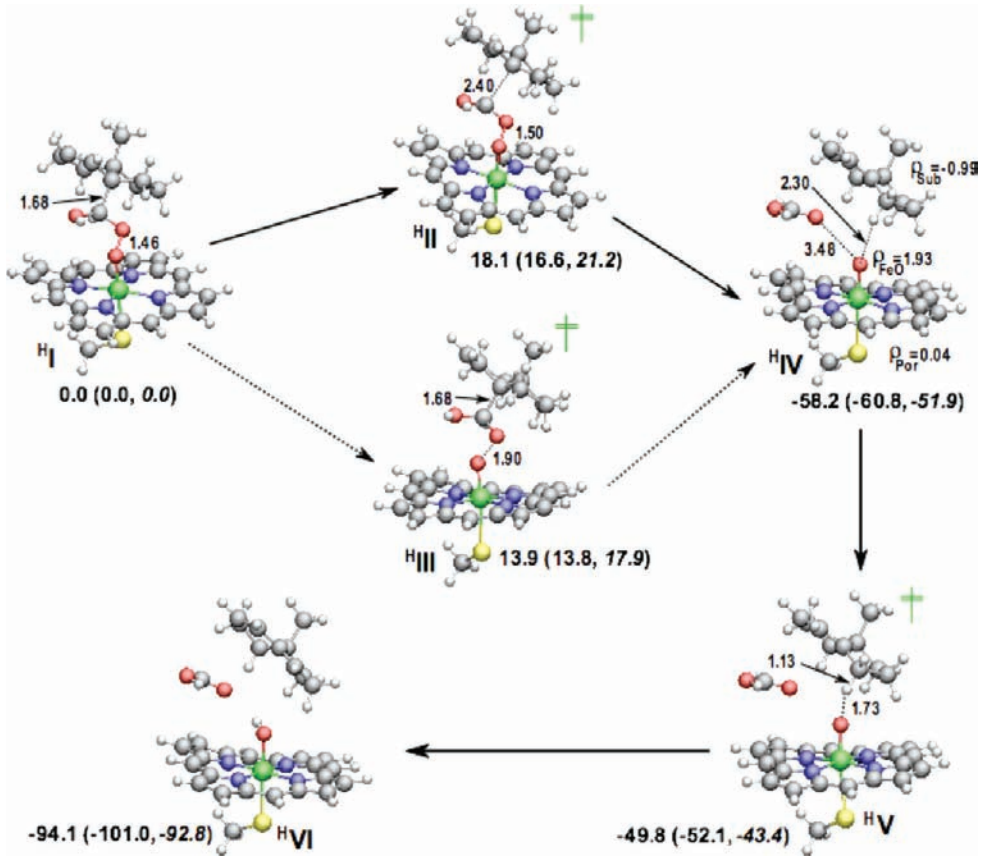

Figure 7. B3LYP/B1:CHARMM mechanism for deformylation of the protonated peroxohemiacetal intermediate. Single-point B3LYP/B2//B1:CHARMM and PBE0/B2//B3LYP/B1:CHARMM (italicized) energies are in parentheses. Energies (kcal/mol) are relative to the protonated peroxohemiacetal species. Spin densities are derived from the B3LYP/B2//B1:CHARMM wave functions. Bond distances are in Å.

of the O−O cleavage transition state are shown in Figure 6B. Since the Cmpd II/deformylated substrate is triradicaloid, O−O bond cleavage therefore occurs as a result of electron transfer from an orbital predominantly localized to the deformylated substrate to an O−O σ^* orbital (Figure 6B, 159 → 161). This event lowers the bond order, facilitating expulsion of formate and formation of Cmpd II from the peroxoformate species.

Introduction of the 14,15 double bond into the steroid backbone and the associated 14α-deformylation proceeds with stereoselective removal of the 15α-hydrogen atom.[66] In the Cmpd II/deformylated substrate/formate complex (Figure 4, **VII**), this atom is poised for abstraction by Cmpd II to complete formation of the experimentally observed products. The transition state for 15α-hydrogen atom abstraction (Figure 4, **VIII**‡) was identified with a corresponding energetic barrier of 8.1 kcal/mol. This transition state is connected to the Cmpd II complex, as well as to the unsaturated steroid, formate, and hydroxy iron protoporphyrin IX (Figure 4, **IX**). This step in the reaction proceeds with an exothermicity of 41.7 kcal/mol. Overall, the stepwise deformylation reaction from the peroxohemiacetal intermediate proceeds with an exothermicity of 105.9 kcal/mol.

A transition state for concerted fragmentation of the peroxohemiacetal was identified and characterized by 15α-hydrogen transfer to the proximal oxygen atom, 10.8 kcal/mol above the peroxohemiacetal species (Figure 4, **III**‡). This transition state connects to the experimentally observed 14,15-unsaturated steroid, formate, and hydroxy iron protoporphyrin IX 92.8 kcal/mol below the peroxohemiacetal intermediate (Figure 4, **IX**). In the absence of the MM partial charge distribution, the energetic barrier and exothermicity of the concerted reaction are similarly 12.0 (10.3) and 104.1 (96.2) kcal/mol at the B3LYP/B2//B1 (PBE0/B2//B3LYP/B1) theoretical level, indicating that the electrostatic environment contributes little to this reaction path. Nonetheless, in light of the near barrierless C−C cleavage in the stepwise mechanism, a concerted mechanism is unlikely to be operative.

3.2.3. Deformylation from the Protonated Peroxohemiacetal. Since Glu173 can shuttle a proton via the hydrogen-bonded water network illustrated in Figure 3A, mechanisms of deformylation branching from the protonated peroxohemiacetal (Figure 7, ^{H}**I**) were also considered. The corresponding intermediates and transition states are illustrated in Figure 7. Transition states for cleavage of both the C−C (Figure 7, ^{H}**II**‡) and O−O (Figure 7, ^{H}**III**‡) bonds were identified with corresponding barriers of 18.1 and 13.9 kcal/mol, respectively. In contrast to the stepwise mechanism elucidated from the deprotonated peroxohemiacetal, these energetic barriers support preferential fragmentation of the O−O bond. Each of these transition states is connected directly to the deformylated substrate/Cmpd II/formic acid complex (Figure 7, ^{H}**IV**). Moreover, no deformylated substrate carbanion intermediate is present on the potential energy surface. Cmpd II is likewise positioned for abstraction of the 15α-hydrogen atom to introduce the 14,15-olefin. Similar to that observed when formate is present, a transition state (Figure 7, ^{H}**V**‡) corresponding to 15α-hydrogen atom abstraction was located corresponding to an energetic

(66) Gibbons, G. F.; Goad, L. J.; Goodwin, T. W. *Chem. Commun.* **1968**, 1458.

barrier of 8.4 kcal/mol. This transition state could be similarly connected to the Cmpd II complex as well as the unsaturated steroid, formic acid, and hydroxy iron protoporphyrin IX (Figure 7, **^{H}VI**). Moreover, the stepwise deformylation reaction proceeds with an exothermicity of 94.1 kcal/mol, analogous to observations when the peroxohemiacetal is deprotonated. In contrast, a transition state corresponding to concerted expulsion of formic acid and introduction of the 14,15-olefin could not be found.

3.2.4. Compound I Mediated Deformylation of the Geminal Diol. A gas phase density functional theory study of a similar reaction, CYP19-catalyzed deformylation, using a truncated model of Cmpd I and the androstenedione C19 geminal diol demonstrated that the latter could be deformylated by an asynchronous, concerted mechanism from the 1β-hydrogen atom abstraction transition state.[23] However, diversion of the proton transfer network and the nucleophilicity of the peroxo intermediate in CYP51 support that Cmpd I formation would be attenuated in the presence of the aldehyde intermediate. Nevertheless, the MD trajectory of the CYP51 Cmpd I/geminal diol intermediate provides an opportunity to investigate the previously described hydrogen-atom abstraction and proton-coupled electron transfer mechanism. The purpose of these calculations is not to directly compare the reactivity of Cmpd I to the peroxo or Cmpd 0 mediated reactions but rather to explore this reaction mechanism in the context of the protein environment.

A myriad of past theoretical studies of Cmpd I mediated oxidation reactions demonstrate that this species has nearly degenerate doublet (^{2}A) and triradicaloid quartet (^{4}A) states. These arise from two electrons of parallel spin occupying π^*_{xz} and π^*_{yz} orbitals on the FeO moiety, while a third electron with parallel or antiparallel spin is localized in an orbital of predominately a_{2u} character on the porphyrin macrocycle.[67−69] Pentaradicaloid quartet (^{4}A′) and sextet (^{6}A) states resulting from a $\delta \rightarrow \sigma^*_{xy}$ electronic excitation in the FeO orbital manifold of the aforementioned triradicaloid states were later demonstrated to contribute to the Cmpd I reactivity in the hydroxylation and epoxidation of propene[70] as well as in the hydroxylation of camphor by CYP101.[71] Drawing from the molecular dynamics trajectory snapshot illustrated in Figure 2A, we explored whether these electronic states of Cmpd I could mediate concerted deformylation of the geminal diol intermediate. The results of these studies are illustrated in Figure 8.

In the CYP51 Cmpd I/geminal diol complex (Figure 8, **^{CmpdI}I**), ^{2}A and ^{4}A are nearly degenerate. Similar to the results of previous calculations,[70,71] the ^{4}A′ and ^{6}A lie 10.4 and 10.7 kcal/mol above ^{2}A, respectively. Removal of the partial charges representing the protein environment changes these energetic spacings by at most 1.6 kcal/mol. However, the protein environment strongly influences the distribution of spin density between the porphyrin macrocycle and methylthiolate ligand. In each state, the protein environment diminishes the absolute spin density on the methyl thiolate while concomitantly increasing porphyrin spin density. For example, in ^{2}A, immersion in the protein pocket results in a $-0.69e \rightarrow -0.13e$ spin density shift on the methylthiolate and $-0.27e \rightarrow -0.83e$ spin density shift on the porphyrin macrocycle. Qualitatively similar trends are observed for the remaining electronic states and levels of theory. A complete list of spin densities calculated in the absence of the electrostatic environment are provided in the Supporting Information.

15α-Hydrogen atom abstraction transition states (Figure 8, **^{CmpdI}II‡**) nascent from Cmpd I were identified and illustrated in Figure 8. In contrast to the energetic spacings for Cmpd I, the transition state energies are greater than 30.4 and 27.2 kcal/mol and compressed within a narrow (2.4 and 2.3 kcal/mol) window at the B3LYP/B1 and B3LYP/B2//B1 levels of theory, respectively. These 15α-hydrogen atom abstraction barriers are larger than those previously reported for various Cmpd I hydrogen atom abstraction reactions.[71−73] Representative of these studies and using a similar B3LYP/CHARMM approach, Altun et al. calculated camphor hydrogen-atom abstraction barriers by CYP101 Cmpd I of 15.8 (17.1) and 22.4 (20.7) kcal/mol for the ^{2}A (^{4}A) and ^{4}A′ (^{6}A) states, respectively.[71] In an effort to elucidate the origins of the higher barriers in CYP51, we removed the partial charge distribution from the MM layer, thereby removing electrostatic interactions with the protein pocket. These calculations revealed an energetic *destabilization* of the transition states by the protein pocket. At the B3LYP/B1 level of theory, removal of the protein environment decreases the hydrogen atom abstraction barriers arising from ^{4}A′ (^{6}A) Cmpd I to 20.8 (20.7) kcal/mol. Moreover, at the B3LYP/B2//B1 level the ^{4}A′ (^{6}A) barriers are decreased to 18.4 (18.4) kcal/mol. Thus, taking the hydrogen atom abstraction barrier in CYP101 as representative for Cmpd I mediated CYP oxidations, the electrostatic environment accounts for nearly all of the destabilization experienced by the pentaradicaloid states. In contrast, the ^{2}A (^{4}A) transition states experience less energetic stabilization with removal of the protein environment with barrier heights of 24.9 (25.4) kcal/mol and 22.7 (23.5) kcal/mol at the B3LYP/B1 and B3LYP/B2//B1 levels of theory, respectively. Notably, both the ^{2}A (^{4}A) and ^{4}A′ (^{6}A) transition states maintain large $\angle$Fe−O−$H_{15\alpha}$ angles (∼162−170°), which are comparable to the "ideal" values in gas phase transition states for propene hydroxylation by the pentaradicaloid states.[70] In contrast, this value is much larger than the "ideal" value (∼135°) for the transition states nascent from the triradicaloid states.[23,70] Distortion of the $\angle$Fe−O−$H_{15\alpha}$ angle is unlikely related to the geminal diol hydrogen bond, since smaller angles were also observed in the gas-phase transition state for 1β-hydrogen atom abstraction from a model androstenedione geminal diol.[23] Thus, despite somewhat less electrostatic destabilization of the transition states nascent from the Cmpd I triradicaloid states, the remaining destabilization energy may be attributed to geometric constraints imparted by the active site. Therefore, together, each of these factors contributes to the near degeneracy of the triradicaloid and pentaradicaloid transition states.

In contrast to the model calculations of the CYP19 reaction, none of these transition states are connected directly to formic acid and the 14,15-unsaturated steroid. Instead, these reaction coordinates encounter an Fe(IV) hydroxy/geminal diol radical intermediate (Figure 8, **^{CmpdI}III‡**). The intermediate complexes are 16.4 and 13.0 kcal/mol above **^{CmpdI}I** and similar to the

(67) Ogliaro, F.; de Visser, S. P.; Cohen, S.; Kaneti, J.; Shaik, S. *ChemBioChem* **2001**, *2*, 848.
(68) (a) Shaik, S.; Kumar, D.; de Visser, S. P.; Altun, A.; Thiel, W. *Chem. Rev.* **2005**, *105*, 2279. (b) Shaik, S.; Cohen, S.; Wang, Y.; Chen, H.; Kumar, D.; Thiel, W. *Chem. Rev.* **2010**, *110*, 949.
(69) de Visser, S. P.; Ogliaro, F.; Sharma, P. K.; Shaik, S. *J. Am. Chem. Soc.* **2002**, *124*, 11809.
(70) Hirao, H.; Kumar, D.; Thiel, W.; Shaik, S. *J. Am. Chem. Soc.* **2005**, *127*, 13007.
(71) Altun, A.; Shaik, S.; Thiel, W. *J. Am. Chem. Soc.* **2007**, *129*, 8978.
(72) Altun, A.; Guallar, V.; Friesner, R. A.; Shaik, S.; Thiel, W. *J. Am. Chem. Soc.* **2006**, *128*, 3924.
(73) Schöneboom, J. C.; Cohen, S.; Lin, H.; Shaik, S.; Thiel, W. *J. Am. Chem. Soc.* **2004**, *126*, 4017.

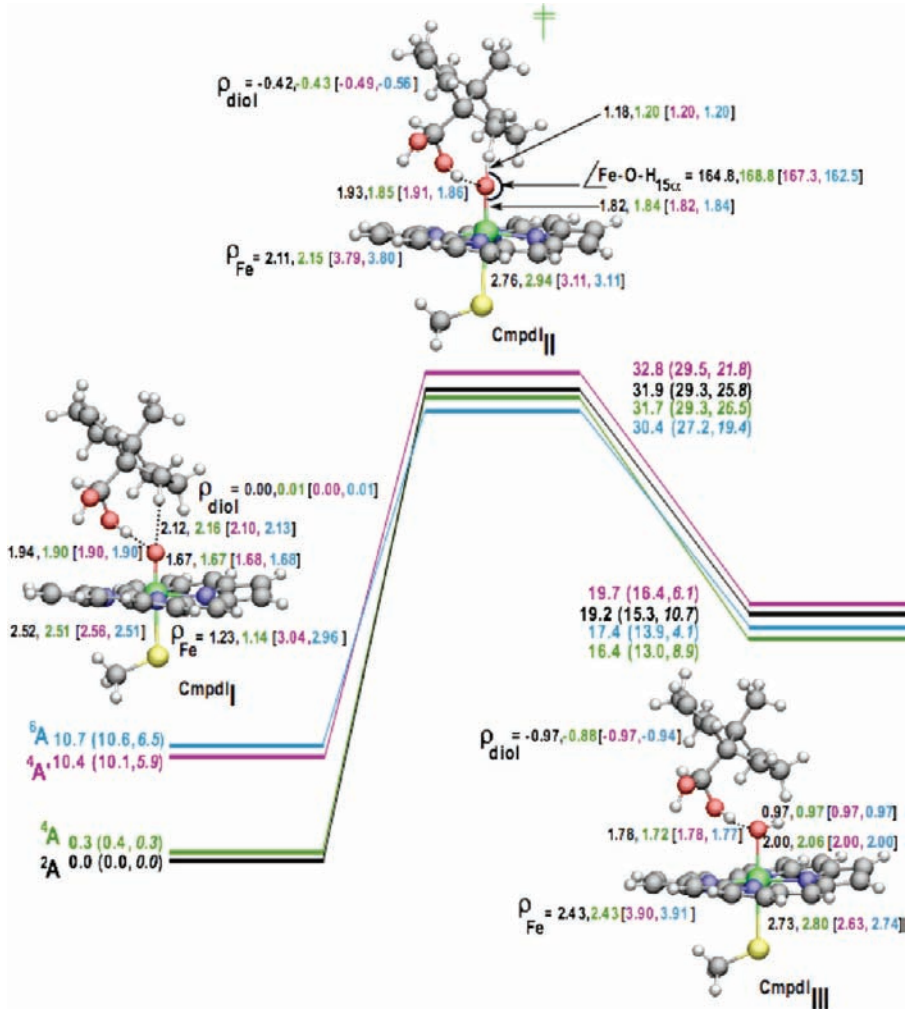

Figure 8. Potential energy surface for 15α-hydrogen atom abstraction from the 3β-hydroxylanosta-8,24-diene-32,32-diol by the triradicaloid (^{2}A, ^{4}A) and pentaradicaloid (^{4}A′, ^{6}A) states of CYP51 Cmpd I. Single-point B3LYP/B2//B1:CHARMM and PBE0/B2//B3LYP//B1:CHARMM (italicized) energies are in parentheses. Energies (kcal/mol) are relative to the ^{2}A Cmpd I species. Spin densities are derived from the B3LYP/B2//B1:CHARMM wave functions. Geometric parameters for the pentaradicaloid states are in square brackets. Bond distances are in Å.

Scheme 3

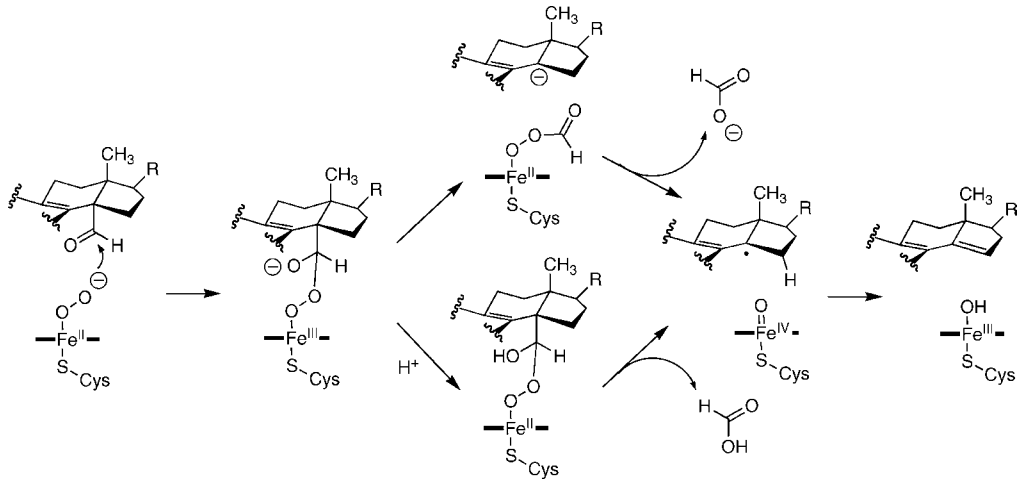

transition states compressed within a narrow energetic window (3.3 and 3.4 kcal/mol) at the B3LYP/B1 and B3LYP/B2//B1 levels of theory, respectively. Compression of these electronic states in the vicinity of the transition states and intermediates supports the profound conclusions of previous studies that excited electronic states become important in Cmpd I mediated oxidation reactions.[70,71]

Relative to the B3LYP/B2//B1 level of theory, calculations with the PBE0 density functional predict smaller energetic spacing between the ^{2}A (^{4}A) and ^{4}A′ (^{6}A) states of Cmpd I,

lower barriers for hydrogen-atom abstraction, and increased stability of the Fe(IV) hydroxy/geminal diol radical intermediate relative to ^{2}A $^{\mathbf{CmpdI}}$**I**. The ^{2}A and ^{4}A states of Cmpd I are nearly degenerate; however, ^{4}A′ and ^{6}A are 4.2 and 4.1 kcal/mol more stable relative to the B3LYP/B2//B1 results. PBE0/B2 stabilizes the transition states and intermediate species arising from the ^{2}A (^{4}A) Cmpd I states by 3.5 (2.8) and 4.6 (4.1) kcal/mol, respectively, relative to B3LYP/B2//B1. However, the relative stabilization is more significant for those species arising from the Cmpd I pentaradicaloid states. In the transition states, the ^{4}A′ (^{6}A) stabilization relative to the B3LYP/B2//B1 level of theory is 7.7 (7.8) kcal/mol. Moreover, in the ^{4}A′ (^{6}A) intermediate this stabilization increases to 10.3 (9.8) kcal/mol. The preferential stabilization of the pentaradicaloid states by the PBE0 functional is roughly correlated with the accumulation of spin density on the Fe atom (Figure 8). Thus, stabilization of these high spin states can be attributed to larger stabilizing effects of d−d exchange interactions at the Fe center. This effect is expected to be more pronounced in the PBE0 calculations because of the larger exact exchange contribution (25%) relative to B3LYP (20%). In agreement, attenuation of the exact exchange contribution in the B3LYP functional to 15% (B3LYP*) destabilizes propene oxidation transition states and intermediates originating from the pentaradicaloid states of Cmpd I.[70]

The possibilty that deformylation might be initiated through hydrogen atom abstraction from one of the geminal hydroxyl groups was also considered. The reaction coordinates for abstraction of this atom from the *pro-R* hydroxyl were mapped from the four electronic states of Cmpd I. From these scans, which are in the Supporting Information, no transition states could be found.

4. Conclusions

Mechanisms for peroxo-mediated deformylation in sterol 14α-demethylase catalysis have been elucidated using a multiscale computational approach. Previous theoretical studies of reactive oxygen catalytic intermediates indicate that Glu173 and a hydrogen-bonded network of water molecules are capable of shuttling the protons necessary for catalysis. The results of the MD simulations described herein suggest that the carboxaldehyde intermediate may divert the hydrogen-bonded network from O_2 in the final catalytic step, affording the peroxo intermediate sufficient lifetime for nucleophilic attack. Diversion of the hydrogen-bond network to the substrate carboxaldehyde does not hinder its function, since protonation of the aldehyde oxyanion is apparently barrierless, concerted, and exothermic. The role of Glu173 in the proton transfer network remains to be experimentally confirmed. Nevertheless, formation of the peroxohemiacetal in the absence of this functional proton shuttle remains energetically favorable. As summarized in Scheme 3, both proton-dependent and -independent reaction paths leading to deformylation were characterized, each supporting the intermediacy of species novel to CYP catalysis. Recent advances in cryoradiolysis of oxyferrous CYPs with spectroscopic techniques to directly observe peroxo and Cmpd 0 intermediates may prove useful for verifying the role of peroxoformate and Cmpd II in the deformylation reaction.[57,74] In the proton-independent path, the enzyme electrostatic environment modulates the electronic structure of the intermediates, illustrating what may be a specific instance of a more widespread phenomenon in CYP catalysis. Parallel studies considering nucleophilic addition of Cmpd 0 to the aldehyde intermediate indicated that this reaction proceeds with high energetic barriers. Furthermore, exploration of the Cmpd I mediated hydrogen-atom abstraction and proton-coupled electron transfer mechanism did not result in an asynchronous, concerted deformylation as described for previous gas phase studies of a similar reaction in CYP19.[23] All of the peroxo-mediated mechanisms described herein are consistent with isotopic labeling data distributions obtained for aromatase[9] and can be applied to interpret experimental data for other C−C bond cleavage reactions. Finally, these studies provide strong theoretical support for alternative oxidants to Cmpd I in CYP-catalyzed reactions.

Acknowledgment. The authors are grateful to the Ohio Supercomputer Center for a generous allocation of computational resources. K.S. was supported by the VCU American Cancer Society Institutional Research Grant.

Supporting Information Available: Cartesian coordinates of atoms in the QM layer, absolute energies, complete population analyses, complete author listing for refs 33 and 42. This material is available free of charge via the Internet at http://pubs.acs.org.

JA906192B

(74) Denisov, I. G.; Mak, P. J.; Makris, T. M.; Sligar, S. G.; Kincaid, J. R. *J. Phys. Chem. A* **2008**, *112*, 13172.